# Microwave Combination Heating: Coupled Electromagnetics- Multiphase Porous Media Modeling and MRI Experimentation

**Vineet Rakesh and Ashim K. Datta**
Dept. of Biological and Environmental Engineering, Cornell University, Ithaca, NY 14853

**Jeffrey H. Walton**
UCD NMR Facility, University of California, Davis, CA 95616

**Kathryn L. McCarthy and Michael J. McCarthy**
Dept. of Food Science and Technology, University of California, Davis, CA 95616

*DOI 10.1002/aic.12659*
*Published online May 23, 2011 in Wiley Online Library (wileyonlinelibrary.com).*

*The work includes development of a multiphase porous media model and magnetic resonance imaging (MRI) experiments to study microwave combination heating. Combination of electromagnetic, convective and radiant heating was considered. The material being heated was modeled as a hygroscopic porous medium with different phases: solid matrix, water and gas, and included pressure driven flow, binary diffusion and phase change. The three-dimensional transport model was fully coupled with electromagnetics to include the effect of variable properties. MRI was used to obtain spatial temperature and moisture distributions to validate the model. The model demonstrated that high and low moisture materials behave differently under different combinations of heating and general guidelines for combining heating modes were obtained. Low moisture materials can be heated effectively using higher microwave power which is not possible in high moisture material. Cycling of microwave was found to be useful in distribution of excessive volumetric heat generated by microwaves.* © 2011 American Institute of Chemical Engineers *AIChE J,* 58: 1262–1278, 2012
*Keywords: microwave combination heating, electromagnetics, magnetic resonance imaging, porous media, heat transfer, mass transfer, finite element method*

## Introduction and Objectives

Combining microwaves with other heating modes such as convection and radiant heating provides an excellent method to speed up heating processes such as cooking,[1] wood drying,[2] processing of ceramics,[3] and pharmaceutical powders,[4] to name a few. Combination heating can potentially provide automated custom-heating ability by implementing precise mix of power sources, their levels and time histories to obtain temperature and moisture profiles needed for specific processes. For example, in the cooking process, the quality of the final product such as texture (e.g., sogginess) or flavor (e.g., browning) is a multifaceted attribute that depends on the temperature and moisture distribution and their time-histories. Through improved understanding of the combination heating process, overheating, underheating, overdrying and sogginess of food can be minimized while enhancing its quality. Reliable prediction of food quality factors will in turn enable increased automation and efficiency in food product and process development. This work proposes to

Correspondence concerning this article should be addressed to A. K. Datta at akd1@cornell.edu.

study combination heating using a fundamental physics-based computational model of the cooking process integrated with complementary magnetic resonance imaging (MRI) experiments to obtain optimum process guidelines for practical use that would provide the desired product quality in the quickest time, paving the way for automation.

### *Previous mathematical models for studying heat and mass transport during electromagnetic heating*

The process of microwave combination heating involves a number of physics and their complex coupling: volumetric electromagnetic heating due to microwaves (solution of Maxwell's equations of electromagnetics), surface heating due to convection and radiant heating, and transport of heat, mass (liquid water, water vapor, air) and momentum inside the sample. Additional complexity arises from the fact that these physics need to be implemented in three-dimensional (3-D) so that volumetric electromagnetic heating is accurately modeled. Computational models to study microwave combination heating to date have not considered all these physics, most of those included heat transfer in the sample only and solved for electromagnetics empirically[5] or using Maxwell's equations.[6–9] Some other studies are for one-dimensional (1-D) or two-dimensional (2-D) cases valid for heating inside a waveguide[8,10–12] only; however for the cavity heating problem considered here, the geometry cannot be reduced to 2-D. Studies that have considered moisture transport have mostly been empirical models[4] using the effective diffusivity formulation.[13,14] However, in case of intensive microwave heating, evaporation and pressure driven flow are significant which these models do not take into account. Only a few studies exist that have considered detailed transport phenomena inside the sample, for example, for deep fat frying[15–17] and wood drying,[18] and even these are an order of magnitude less complex compared to the present study since they did not involve electromagnetic heating. On the other hand, empirical models have been used for electromagnetic heating when present.[19,20] In this study, we develop a fundamental physics based model that can be applied to generic processes that include electromagnetic heating and heat and mass transfer inside the sample. The model includes the solution of Maxwell's equations of electromagnetics in 3-D to obtain the electric field inside the oven cavity and the sample. A 3-D multiphase porous media model based on conservation laws is formulated to describe the heat, mass and momentum transfer inside the sample. The electromagnetics and multiphase porous media models are then fully coupled to model the combination heating process. Note that it can also be thought of as a combination drying process and its applicability extends to many heating processes such as drying, baking and thawing used in the food industry and elsewhere.

### *Modeling of materials with variable properties*

Many industrial materials such as metal oxide ceramics and polymers exhibit a phenomena known as thermal runaway[21,22] where dielectric properties change rapidly with temperature thereby considerably affecting the heating patterns in the sample due to microwave irradiation. In foods, dielectric properties are functions of temperature and moisture. Therefore, the computational model, in addition to accounting for all the different physics, should be fully coupled so that it can go back and forth between different physics (electromagnetics and transport) and update time dependent property values as needed. This is yet another modeling challenge that has not been addressed previously. Prior models that included dielectric property change are for simpler cases which considered heat transfer only[23] or did not solve the Maxwell's equations.[24] In this work, we develop a fully coupled model that includes a property updating scheme so that the model can work effectively for a wide variety of materials including thermal runway materials.

### *Experimental measurement and validation techniques used previously*

It is critical not only to formulate a systematic modeling approach that accounts for all the physics occurring in the sample but to also have a sophisticated experimental technique to validate the computational model. Detailed and accurate measurement of volumetric electromagnetic heating can be obtained from 3-D mapping of heating profiles using a technique such as Magnetic Resonance Imaging (MRI).[25] Although a few studies have looked at detailed measurement and validation techniques using MRI,[6,26] most of these have reported temperature distributions only. Others have used techniques such as measurement of surface temperatures using infrared camera[7] or thermosensitive paper[27] and point temperature measurement using fiber optic temperature probe[28] that do not give a complete picture of the 3-D heating process involving volumetric electromagnetic heating. Moisture movement and distribution is critical to the quality of the final product as discussed above; however, quantitative distribution of moisture in 3-D has not been reported earlier.[29–31] In this study, we not only include the mapping of temperatures but moisture as well using MRI that again presents inherent challenges. The computational model is comprehensively validated by comparison with the experimental temperature and moisture profiles.

### *Objectives*

The main objectives of this study are to: (1) Formulate and solve a fundamental physics based mathematical model for combination heating processes; (2) Use magnetic resonance imaging (MRI) measurements for fundamental understanding of the process and to validate the computational model; (3) Use the computational model to test "what-if" scenarios during combination heating with the aim of design and optimization of the process.

The manuscript is organized as follows. First, the mathematical formulation consisting of electromagnetics and multiphase porous media models is presented and the solution strategy is discussed. Subsequently, the experimental methodology that includes the combination oven, test material and MRI details is discussed. The model is then validated using the MRI results and its predictions are used to understand different combination heating processes.

## Mathematical Model

Mathematical description of the combination heating process broadly requires the solution of two different physics-electromagnetics in the oven cavity and sample, and heat, mass and momentum transport in the sample. The Maxwell's equations of electromagnetics are solved to obtain the electric field inside the oven cavity and sample, and coupled with a multiphase porous media model to obtain temperature and moisture distribution in 3-D inside the samples. These different physics are discussed in details separately in the following sections.

### *Electromagnetics—Solution of Maxwell's equations in the oven cavity and sample*

The Maxwell's equations of electromagnetics for variable dielectric properties are given by

$$\nabla \times \mathbf{E} = -j\omega\mu_0\mathbf{H} \tag{1}$$

$$\nabla \times \mathbf{H} = j\omega\epsilon_0\epsilon\mathbf{E} \tag{2}$$

$$\nabla \cdot \epsilon\mathbf{E} = 0 \tag{3}$$

$$\nabla \cdot \mathbf{H} = 0 \tag{4}$$

where $\mathbf{E}$ is the electric field intensity and $\mathbf{H}$ is the magnetic field intensity, both defined as time harmonics

$$\mathbf{E}(x,y,z,t) = \mathbf{E_0}(x,y,z)\ e^{i\omega t} \tag{5}$$

$$\mathbf{H}(x,y,z,t) = \mathbf{H_0}(x,y,z)\ e^{i\omega t} \tag{6}$$

The complex relative permittivity, $\epsilon$, of the dielectric material (model food product) is given by

$$\epsilon = \epsilon' + i\epsilon'' \tag{7}$$

where $\epsilon'$ is the dielectric constant and $\epsilon''$ is the dielectric loss factor. For these materials, we do not expect the magnetic susceptibility to vary.

*Boundary Condition.* The combination oven walls were perfect electric conductors. Therefore

$$E_{\text{tangential,oven wall}} = 0 \tag{8}$$

*Microwave Heating Term.* The heat absorbed by the sample per unit time due to the microwaves is given by

$$Q(x,y,z,t) = \frac{1}{2}\omega\epsilon_o\epsilon''|\mathbf{E}|^2 \tag{9}$$

### *Multiphase porous media model—Transport of momentum, mass and energy in the sample*

To describe the heat, mass and momentum transfer in the sample during the combination heating process, a 3-D multiphase porous media model was formulated. The sample was considered as a porous material[32] with three phases: solid, liquid water and gas. The gas phase had two components: water vapor and air. The schematic of a representative elementary volume (REV) of the material is shown in Figure 1.

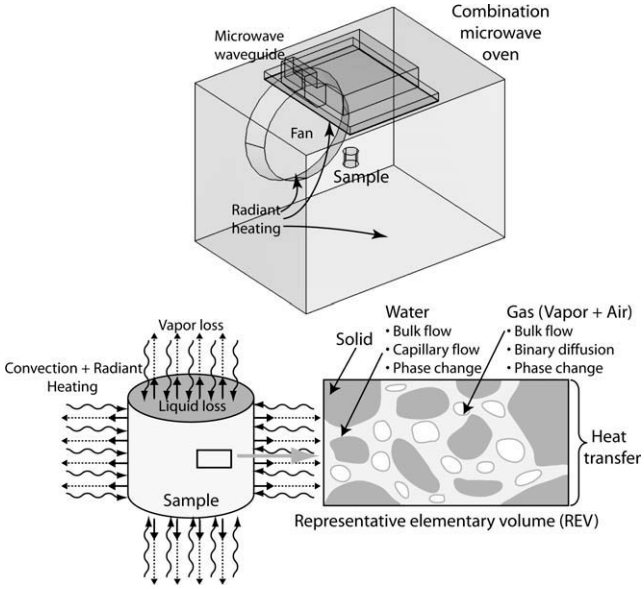


**Figure 1. (a) The computational domain for the electromagnetic simulation (for microwave heating) consists of both the oven and the sample; (b) porous media model was solved only inside the sample as shown.**

Also shown are the boundary conditions on the surface of the sample.

The volume fraction of pores in a representative elementary volume of the material, $\Delta V$, is denoted by porosity, $\phi$

$$\phi = \frac{\Delta V_p}{\Delta V} = \frac{\Delta V_w + \Delta V_g}{\Delta V} \tag{10}$$

where $\Delta V_w$ and $\Delta V_g$ are the volume occupied by liquid water and gas phases in the REV respectively. The structure of the sample does not change during the combination heating process (verified experimentally) and hence the porosity remains constant.

The mass conservation equation for the transportable phases includes the effects of bulk flow (convection), diffusion and capillary flow. The porous media model also incorporates the change of phase between liquid water and vapor (evaporation/condensation) throughout the domain. The energy conservation equation is solved for the mixture and the effect of microwave heating is included as a source term obtained from the electromagnetics model.

### *Momentum conservation*

Darcy's law is valid for flow in the porous media where velocities are low. The superficial velocity for each moving phase (liquid water and gas) due to the gas pressure gradient in the medium is therefore given by

$$\mathbf{v_{sup,i}} = -\frac{k_i k_{r,i}}{\mu_i}\nabla P \tag{11}$$

where $i = w$ denotes the liquid water phase and $i = g$ the gas phase. The total gas pressure is the sum of the partial pressures

of vapor and air based on the ideal gas law, $P = p_a + p_v$. The actual velocity due to the gas pressure for each phase based on the volume occupied by that particular phase is therefore given by

$$\mathbf{v_i} = -\frac{1}{S_i\phi}\frac{k_i k_{r,i}}{\mu_i}\nabla P \tag{12}$$

where $S_w$ and $S_g$ are the liquid water saturation and gas saturation, respectively. The saturations, $S_i$, denote the volume fraction of the liquid or gas phase with respect to pore volume

$$S_i = \frac{\Delta V_i}{\Delta V_p} = \frac{\Delta V_i}{\phi \Delta V} \tag{13}$$

Liquid water in the pores experience the capillary pressure, $p_c$, in addition to the gas pressure. Therefore

$$p_w = P - p_c \tag{14}$$

The effective velocity of the liquid phase is therefore given by

$$\begin{aligned}\mathbf{v_{eff,w}} &= -\frac{1}{S_w\phi}\frac{k_w k_{r,w}}{\mu_w}\nabla p_w \\ &= -\frac{1}{S_w\phi}\frac{k_w k_{r,w}}{\mu_w}\nabla P + \frac{1}{S_w\phi}\frac{k_w k_{r,w}}{\mu_w}\nabla p_c \\ &= \mathbf{v_w} + \frac{1}{S_w\phi}\frac{k_w k_{r,w}}{\mu_w}\frac{\partial p_c}{\partial S_w}\nabla S_w\end{aligned} \tag{15}$$

Equation 15 can be written in terms of capillary diffusivity,[33] $D_c = -\frac{k_w k_{r,w}}{\phi\mu_w}\frac{\partial p_c}{\partial S_w}$, and water concentration, $c_w = \rho_w \phi S_w$, in a compact form

$$\mathbf{v_{eff,w}} = \mathbf{v_w} - \frac{D_c}{c_w}\nabla c_w \tag{16}$$

### *Mass conservation*

The mass conservation equation for the liquid water phase includes the bulk flow and phase change

$$\begin{aligned}\frac{\partial c_w}{\partial t} + \nabla\cdot\left(\mathbf{v_{eff,w}}c_w\right) &= -\dot{I} \\ \frac{\partial c_w}{\partial t} + \nabla\cdot\left(\mathbf{v_w}c_w\right) &= \nabla\cdot\left(D_c\nabla c_w\right) - \dot{I}\end{aligned} \tag{17}$$

The continuity equation for the gas phase is given by

$$\frac{\partial c_g}{\partial t} + \nabla\cdot\left(\mathbf{v_g}c_g\right) = \dot{I} \tag{18}$$

The mass conservation equation for the vapor component of the gas phase includes bulk flow, binary diffusion and phase change

$$\frac{\partial c_v}{\partial t} + \nabla\cdot\left(\mathbf{v_g}c_v\right) = \nabla\cdot\left(S_g\phi\frac{C^2}{\rho_g}M_a M_v D_{\mathrm{eff,g}}\nabla x_v\right) + \dot{I} \tag{19}$$

Here, vapor concentration is related to the gas concentration by its mass fraction, $c_v = \omega_v c_g$. Similarly, concentration of air, $c_a$, is $\omega_a c_g$. Knowing the mass fraction of vapor from Eq. 19, mass fraction of air can be calculated from the expression

$$\omega_a = 1 - \omega_v \tag{20}$$

### *Energy conservation*

Energy conservation includes convection due to moving phases, conduction, phase change and microwave heat source term calculated from Eq. 9

$$\begin{aligned}&\left[\sum_{i=s,w,v,a}\left(c_i c_{p,i}\right)\right]\frac{\partial T}{\partial t} + c_i\mathbf{v_i}\cdot\nabla\left[\sum_{i=w,v,a}\left(c_{p,i}T\right)\right] \\ &\quad - D_c\nabla c_w\cdot\nabla\left(c_{p,w}T\right) = \nabla\cdot\left(k_{\mathrm{eff}}\nabla T\right) - \lambda\dot{I} + Q(x,y,z,t)\end{aligned} \tag{21}$$

Here, the effective thermal conductivity is given by the volume weighted average of the different phases and components

$$k_{\mathrm{eff}} = (1-\phi)k_s^{th} + \phi\left\{S_w k_w^{th} + S_g\left(\omega_v k_v^{th} + \omega_a k_a^{th}\right)\right\} \tag{22}$$

### *Phase change (evaporation/condensation)*

The formulation for phase change is obtained from the literature[15]

$$\dot{I} = K\frac{M_v}{RT}\left(p_{v,eq} - p_v\right) \tag{23}$$

where $p_{v,eq}$ is the equilibrium vapor pressure which is a function of both temperature and moisture content of the material.

### *Boundary and initial conditions*

The boundary conditions needed to solve the set of governing equations are now listed (also shown in Figure 1). Pressure was set to ambient at all surfaces of the cylindrical sample

$$P\big|_s = P_{amb} \tag{24}$$

Water from the interior can move out of the boundary as vapor after evaporation. When the liquid water saturation becomes high ($S_w = 1$), water can also move out of the open surfaces directly by drip flow. Therefore

$$j_{n,w}\big|_s = h_m\phi S_w\left(\rho_v - \rho_{v,\mathrm{oven}}\right) + \underbrace{c_w v_{n,w}}_{\text{when } S_w = 1} \tag{25}$$

where $j_{n,w}$ is the total normal flux of water at a particular surface. Vapor can be convected away from the open surfaces. Therefore

$$j_{n,v}\big|_s = h_m\phi S_g\left(\rho_v - \rho_{v,\mathrm{oven}}\right) \tag{26}$$

Convection and radiant heating act only on the surface and are, therefore, included as boundary conditions while solving the energy conservation equation. The loss of heat due to evaporation of water, removal of liquid water (during drip

flow) and vapor is also included in the boundary condition for heat transfer

$$q_n\big|_s = h(T - T_{\text{oven}}) - h_m\phi S_w(\rho_v - \rho_{v,\text{oven}})\lambda - h_m\phi(S_w + S_g)(\rho_v - \rho_{v,\text{oven}})\, c_{p,v}T - \underbrace{c_w v_{n,w}\, c_{p,w}T}_{\text{when } S_w=1} \quad (27)$$

where $q_n$ is normal heat flux.

*Initial Conditions.* The initial conditions for the different variables are listed in the input parameters table (Table 1).

### *Input parameters*

All input parameters used for the simulations are listed in Table 1. The heating modes considered are detailed in Table 2.

### *Numerical solution*

The schematic of the computational domain along with the different physics solved for in the subdomains are shown in Figure 1. The entire oven had to be modeled since it is not symmetric in any direction due to the presence of the fan on the back wall and waveguide on the top (Figure 1a). The governing equations for electromagnetics and porous media model need to be fully coupled. The coupling of physics and the solution process are illustrated in Figure 2 and are now discussed in detail. As temperature and moisture distribution in the material changes with heating time, the dielectric properties change (as given by the relations in Table 1). This in turn changes the electric field distribution inside the oven and sample and as a result, the microwave power absorbed (source term in the heat equation) by the sample changes and electromagnetic simulations have to be repeated to determine the updated microwave source term. Additionally, different finite element meshes for the electromagnetics and heat transfer problems are needed that requires mapping of solution back and forth between the different meshes, different solvers for the two physics and specification of coupling parameters also need to be included. To incorporate this coupling, the electromagnetics and porous media problems were independently setup in COMSOL Multiphysics (COMSOL, Burlington, MA) graphical user interface (GUI). A code was then written in scripting version of the software, COMSOL Script, to implement the feedback mechanism. The electromagnetics problem was solved using the GMRES iterative solver with the Geometric Multigrid preconditioner. The mesh consisted of a total of 367,082 tetrahedral elements based on mesh convergence study. For solving the energy equation, the UMFPACK direct solver was used with the sample discretized into 44,865 elements. The solver selection for the two physics, solution updating interval and mapping of the electromagnetic solution to the heat transfer mesh and vice versa were programmed in the code. The electromagnetics solution update interval can be set in the code based on the relative change in dielectric properties between two time steps while solving the transport problem. For materials that exhibit thermal runway, the solution update interval will be small. However, the thermal runway effect was not observed for the material considered in this study. The simulations were run on a 3 GHz Windows workstation with 16 Gb memory.

## Experimental Methodology

Details about the combination oven used, heating protocol, test material, magnetic resonance imaging and other experiments for input parameter measurement are discussed.

### *Microwave oven and heating protocol*

Heating was performed in a GE Combination Oven (Model No. JT930BHBB, General Electric Company, Louisville, KY) located at the UC Davis NMR Facility. It was equipped for convection-radiant and combined convection-radiant and microwave heating modes. Two different settings of the oven representing different heating combinations were selected for the experiments, one without microwaves and the other with microwaves. The oven temperature for the convection-radiant heating combination was set at 80°C. For the microwave assisted heating combination, the oven temperature was also set at 80°C and microwave heating was on for 10 s for a 50 s cycle. These heating rates were chosen so that there was no significant deformation in the samples. For each of the two heating combinations, samples were heated for 10, 15, 20, and 30 min. These are also listed in Table 2. Two replicates were performed for each heating combination. Samples were heated one at a time at the center of the oven by placing them on a 5 cm diameter polysulfone disc in a petri dish to minimize direct heating from the oven rack. After combination heating of the sample, it was transferred to a 50 mL pyrex beaker that fit into the sample holder for the imaging spectrometer.

### *Test material*

The model product was rehydrated Wegmans Instant Mashed Potatoes (Wegmans Food Markets, Rochester, NY). For each batch, 125 g of potato flakes (moisture content of 0.068 wb) was mixed with 550 g hot (95–100°C) distilled water. The potato flakes and water were mixed thoroughly and the mixture was allowed to equilibrate for 14 h in a 20°C incubator to obtain a uniform consistency for MRI imaging. This also avoided anisotropy in the material properties of the sample. Samples were prepared by placing the mixture in mesh cylinder container with 3.66 cm internal diameter and 3.5 cm height. The mesh cylinders material was PTFE (polytetrafluoroethylene) (ET8500, Industrial Netting, Minneapolis, MN) that was suitable for high temperature applications and minimum interference with the microwaves. Sample heating and magnetic resonance imaging commenced within an hour of sample preparation.

### *Magnetic resonance imaging (MRI) measurements*

MRI experiments were performed at the UC Davis NMR Facility using a 7T super-conducting magnet and Biospec console (Bruker Biospin MRI, Billerica, MA) with 300 MHz for $^1$H-resonance frequency. Three NMR protocols[36] were used: gradient echo sequence (Fast Low Angle Shot, FLASH), Multislice multiecho sequence (MSME), and Carr Purcell Meiboom Gill sequence (CPMG). The NMR parameters are given in Table 3. The FLASH sequence was used to generate temperature maps; the MSME was used to generate spin-spin relaxation time ($T_2$) maps and $M_0$ maps. CPMG

**Table 1. Input Parameters for the Simulations**

| Parameter | Value | Source |
|---|---|---|
| Oven dimensions (m) | $0.61 \times 0.44 \times 0.44$ | |
| Sample (cylindrical) dimensions (m) | 0.018 (rad) $\times$ 0.035 | |
| Electromagnetics | | |
| Microwave frequency (GHz) | 2.45 | |
| Dielectric constant, $\epsilon'$ | $27.403 + 9.5387M - 0.6018M^2$ | |
| Dielectric loss, $\epsilon''$ | $23.756 - 4.8009M + 0.3613M^2$ | |
| Transport | | |
| Porosity, $\phi$ | 0.88 | 16 |
| Viscosity | | |
| Water, $\mu_w$ (Pa s) | $0.988 \times 10^{-3}$ | |
| Vapor and air, $\mu_g$ (Pa s) | $1.8 \times 10^{-5}$ | |
| Intrinsic permeability | | |
| Water, $k_w$ ($m^2$) | $5 \times 10^{-14}$ | 16 |
| Vapor and air, $k_g$ ($m^2$) | $10 \times 10^{-14}$ | 16 |
| Relative permeability | | |
| Water, $k_{r,w}$ | $[(S_w - 0.09)/0.91]^3$, $S_w > 0.09$<br>0, $S_w < 0.09$ | 32 |
| Vapor and air, $k_{r,g}$ | $1 - 1.1S_w$, $S_w < 1/1.1$<br>0, $S_w > 1/1.1$ | 32 |
| Capillary diffusivity (water), $D_c$ ($m^2/s$) | $10^{-8} \exp(-2.8 + 2M)$ | 16 |
| Binary diffusivity, $D_{eff,g}$ ($m^2/s$) | $2.6 \times 10^{-6}$ | |
| Specific heat capacity | | |
| Solid, $c_{ps}$ (J/kg K) | 1650 | 34 |
| Water, $c_{pw}$ (J/kg K) | 4178 | 34 |
| Vapor, $c_{pv}$ (J/kg K) | 2062 | 34 |
| Air, $c_{pa}$ (J/kg K) | 1006 | 34 |
| Thermal conductivity | | |
| Solid, $k_s^{th}$ (W/m K) | 0.21 | 34 |
| Water, $k_w^{th}$ (W/m K) | 0.57 | 34 |
| Vapor, $k_v^{th}$ (W/m K) | 0.026 | 34 |
| Air, $k_a^{th}$ (W/m K) | 0.026 | 34 |
| Density | | |
| Solid, $\rho_s$ ($kg/m^3$) | 1430 | |
| Water, $\rho_w$ ($kg/m^3$) | 998 | |
| Vapor, $\rho_v$ ($kg/m^3$) | Ideal gas law | |
| Air, $\rho_a$ ($kg/m^3$) | Ideal gas law | |
| Latent heat of vaporization, $\lambda$ (J/kg) | $2.26 \times 10^6$ | |
| Evaporation rate constant, $K$ (/s) | $1 \times 10^{-3}$ | |
| Equilibrium vapor pressure, $p_{v,eq}$ (Pa) | $p_{sat}(T)\exp(-0.0267M^{-1.656}$<br>$+0.0107e^{-1.287M}M^{1.513}\ln[p_{sat}(T)])$ | 35 |
| Ambient pressure, $P_{amb}$ (Pa) | 101,325 | |
| Mass transfer coefficient, $h_m$ (m/s) | $6 \times 10^{-3}$ | |
| Heat transfer coefficient, $h$ ($W/m^2$ K) | | |
| Top | 80 | |
| Side | 20 | |
| Oven temperature, $T_{oven}$ (°C) | 80 | |
| Initial Conditions | | |
| Pressure, $P_0$ (Pa) | 101,325 | |
| Water concentration, $c_{w,0}$ ($kg/m^3$) | 789.4 | |
| Vapor mass fraction, $\omega_{v,0}$ | 0.01 | |
| Temperature, $T_0$ (°C) | 22 | |

verified the mono-exponential decay of the relaxation time ($T_2$).

For each sample, the sequence of NMR data acquisition was FLASH, MSME, CPMG for the sample at room temperature and then FLASH, MSME, CPMG for the same sample after heat treatment. Data was acquired over a time frame of 4.5 min for the sequence (FLASH, MSME, CPMG). The samples were positioned identically in the magnet for the imaging procedure before and after heat treatment. Temperatures at different locations were calculated by measuring the phase shift using MRI and then using the following expression

**Table 2. Different Combination of Heating Modes Considered**

| Heating Modes | Air Temperature, (°C) | MRI measurement, (min) |
|---|---|---|
| Convection, radiant | 80 | 10, 15, 20, 30 |
| Cycled microwaves (cycling: 10 s ON, 40 s OFF), convection, radiant | 80 | 10, 15, 20, 30 |
| Full microwaves, convection, radiant | 80 | – |

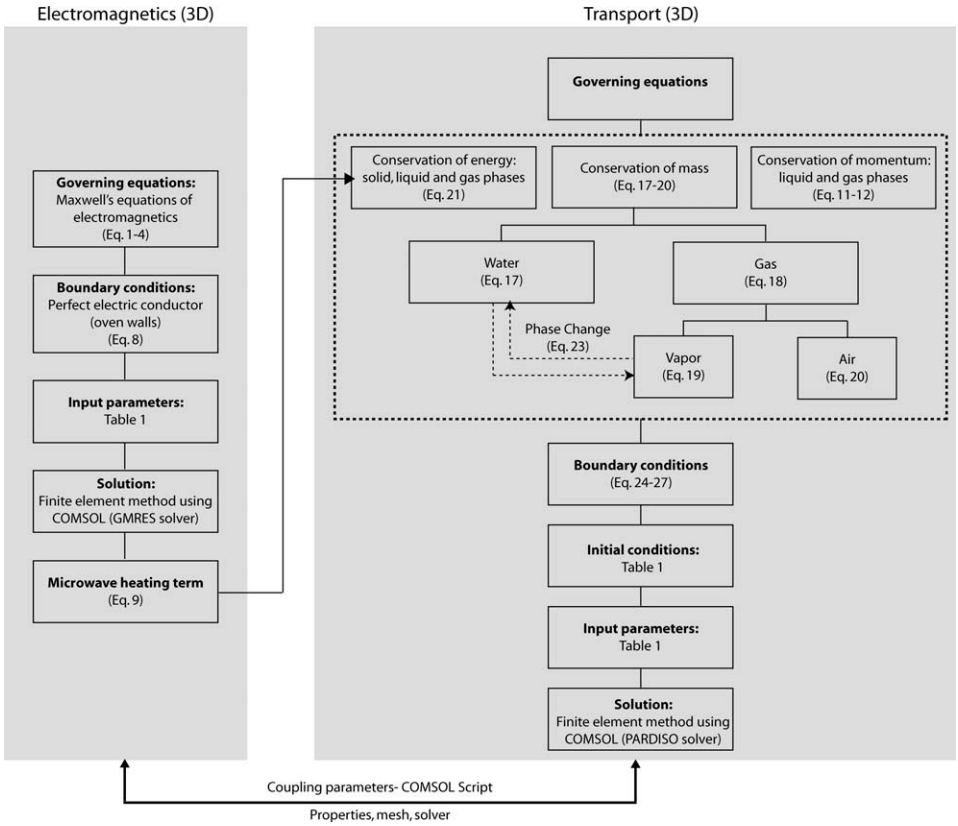


**Figure 2. Flow chart showing the sequence of steps followed to develop the computational model.**

$$\Delta T = \frac{\varphi - \varphi_{\text{ref}}}{\alpha\gamma(TE)B_o} \tag{28}$$

where $\varphi$ is the phase value after heating, $\varphi_{\text{ref}}$ is the phase value before heating, $B_o$ is the magnetic field strength, $\alpha$ is the proportionality constant, TE is the echo time and $\gamma$ is the magnetogyric ratio of hydrogen nucleus. The $M_0$ values obtained from MRI were correlated to moisture content measured using gravimetric analysis (described in the next section). The temperature and moisture maps represented 12 horizontal slices from the bottom to top of the cylindrical sample as shown in Figure 3.

A Matlab code was utilized for creating temperature maps based on Eq. 28. The temperature images were calculated using a voxel by voxel subtraction of the phase images after and before heating. Before subtraction, the individual phase images had phase accumulations greater than $2\pi$ resulting in phase discontinuities; these were removed before subtraction by adding $2\pi n$ (where $n$ is an integer). The resulting temperature images were smoothed using a five point median filter to reduce the influence of noise.

**Table 3. MRI Parameters for the Experiments**

| MRI Parameters | MSME | FLASH |
|---|---|---|
| TE (ms) | 8.527 | 3.264 |
| No. of echoes | 16 | NA |
| Flip angle (°) | NA | 20 |
| TR (ms) | 10,000 | 89.6 |
| Matrix size | 128 × 128 | 128 × 128 |
| FOV ($mm^2$) | 64 × 64 | 64 × 64 |
| No. of slices | 12 (Coronal orientation) | 12 (Coronal orientation) |
| Slice thickness | 3 mm | 3 mm |

### *Gravimetric measurement of moisture loss for correlation with MRI signal intensities*

Moisture loss due to the heating process was determined using gravimetric measurement. Each sample was weighed before heating at room temperature and immediately following the combination heating process. These measurements were correlated with the $M_0$ values obtained from MRI.

### *Input parameter measurements*

Dielectric properties and heat transfer coefficients for modeling the convection-radiant heating were measured experimentally. Other input parameters for the sample were

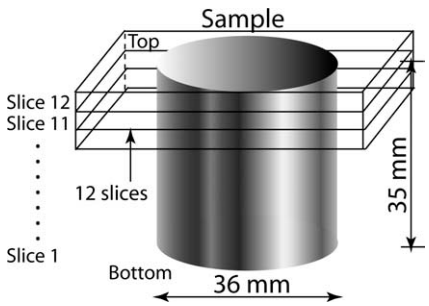


**Figure 3. Orientation of the slices obtained using MRI.**

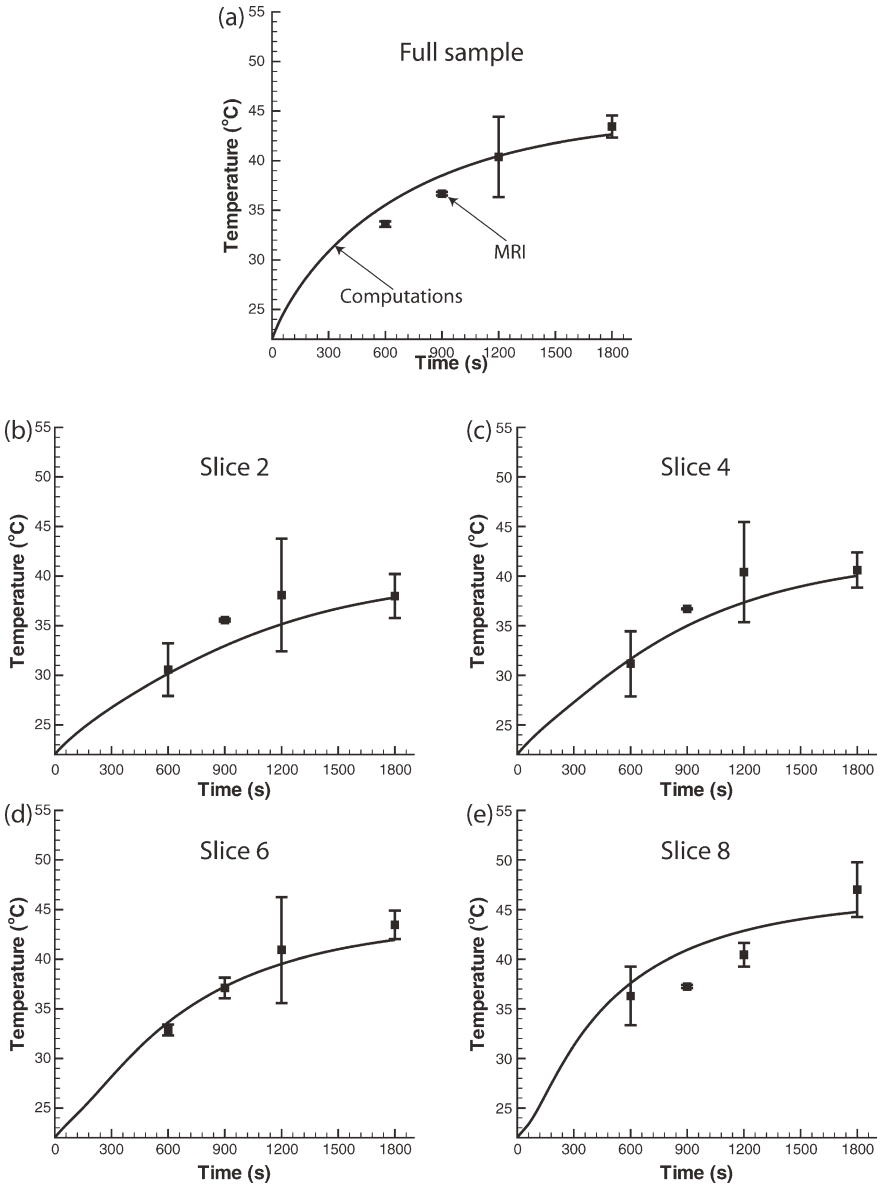


**Figure 4. Comparison of temperatures at different times obtained from computations and MRI experiments for the heating combination that involved convection and radiant heating only (no microwaves).**

The topmost plot shows the average temperature comparison for the full sample and the other plots show the comparison for four different slices (temperatures averaged over slices 2, 4, 6, and 8 of the 12 slices). MRI slice orientation is shown in Figure 3.

obtained from literature and are shown in Table 1. All material properties were isotropic.

*Dielectric Properties.* The dielectric properties (dielectric constant and loss) of the samples were measured as a function of moisture content at the microwave frequency of 2.45 GHz using HP85070 open ended coaxial high-temperature probe (Agilent Technologies) and a network analyzer (Agilent 8722ES).

*Heat Transfer Coefficients.* Point temperature and heat flux histories were measured by thermocouples and heat flux sensors (HFS-3, Omega) connected to FLUKE data acquisition Bucket (Fluke). The heat transfer coefficients for different heating modes were calculated using the values of heat flux, surface temperature, and ambient oven temperature.

## Results and Discussion

Experimental validation of the mathematical model is presented for two different combinations of heating, followed by descriptions of temperature, moisture and pressure distributions in the sample for various heating combinations and initial moisture content of the sample. To comprehensively understand the process of combining the different modes of heating for different materials, the variables that affect the final product such as temperature, moisture content and pressure in the domain obtained from computations are analyzed in detail for different conditions. Three different heating combinations were considered, as listed in Table 2: convection + radiant heating; cycled microwave + convection + radiant

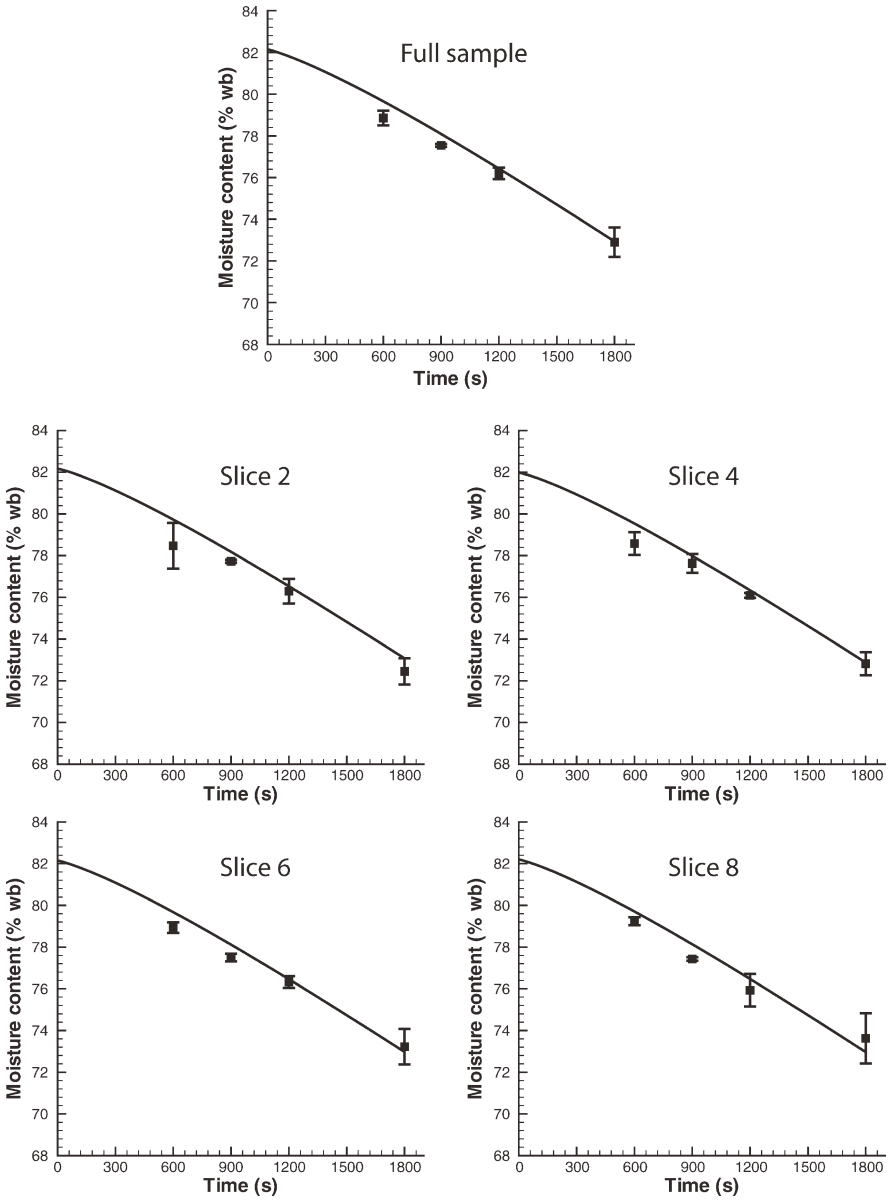


**Figure 5. Comparison of moisture contents at different times obtained from computations and MRI experiments for the heating combination that involved convection and radiant heating only (no microwaves).**

The topmost plot shows the average moisture content comparison for the full sample and the other plots show the comparison for four different slices (moisture contents averaged over slices 2, 4, 6, and 8 of the 12 slices). MRI slice orientation is shown in Figure 3.

heating; and full microwave + convection + radiant heating. Samples at two different initial moisture contents of 82.1% wb (4.6 db) and 69.7% wb (2.3 db) were heated using these different combinations and the comparisons are presented.

### *Experimental validation of temperature and moisture*

Experimental validation is critical considering the complexity of the computational model. Validation was done by comparing the temperature and moisture content predicted by the model with the corresponding experimental values obtained from MRI measurements for the different heating combinations, as shown in Figures 4–7. These comparisons were done for two heating scenarios: the first included convection and radiant heating only and the other heating combination comprised of microwave (cycled), convection and radiant heating. Details of heating combinations are shown in Table 2.

*Convection + Radiant Heating.* The top subplot (i.e., Figure 4a) compares the computed and measured average temperature or moisture history for the full sample during the combination heating process. The other four subplots (Figures 4b–e) present average temperature and moisture histories at four different sections (slice orientation are shown in Figure 3). All computed values were obtained using volume averaging. For convection and radiant heating (Figure 4), both experiments and computations show that greater heating is from the top of the sample which is exposed to

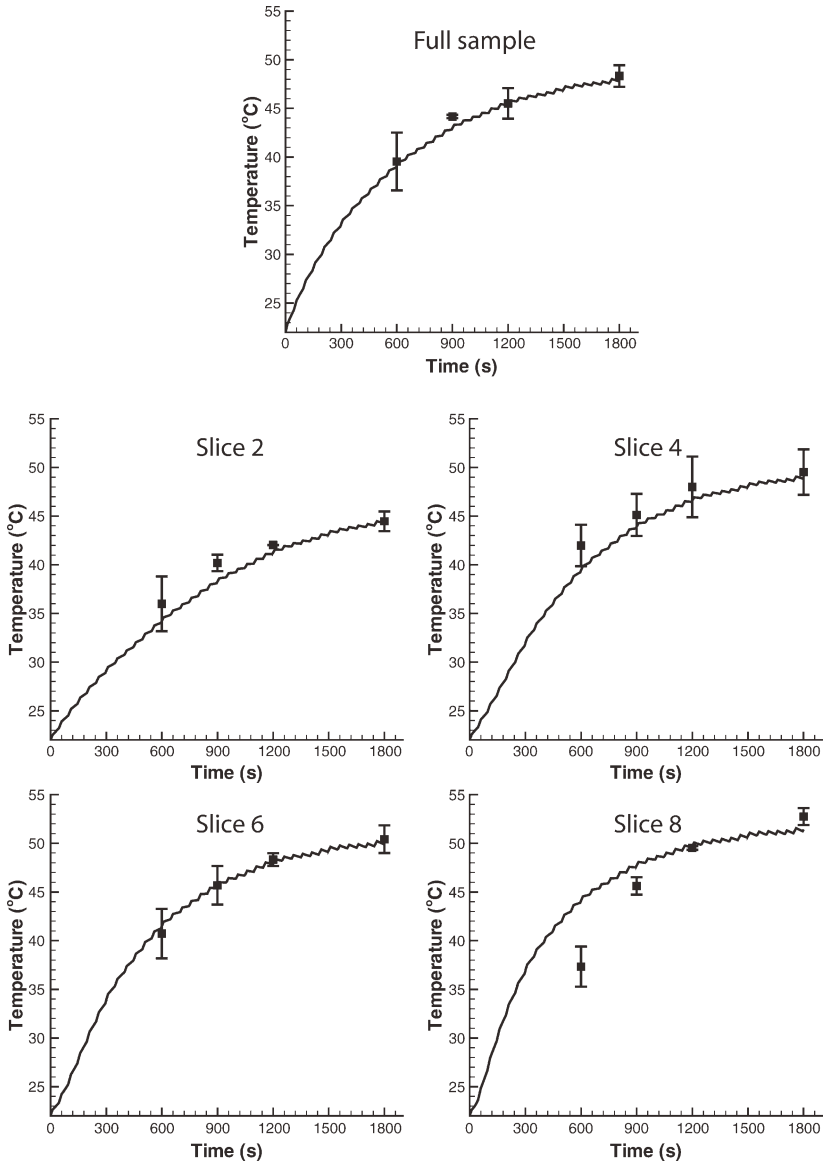


**Figure 6. Comparison of temperatures at different times obtained from computations and MRI experiments for the heating combination that involved convection, radiant heating and microwaves.**

The topmost plot shows the average temperature comparison for the full sample and the other plots show the comparison for four different slices. MRI slice orientation is shown in Figure 3.

the hot air. Moisture, on the other hand, is lost uniformly from the sample, as shown in Figure 5. This is attributed to very high initial moisture content (~82% w.b.) and therefore, moisture loss depends entirely on the external resistance (as determined by the mass transfer coefficient). However, this is true only for this particular case where the initial moisture content is high and not in the low moisture case discussed later in the paper in detail.

*Cycled Microwave + Convection + Radiant Heating.* In case of microwave combination heating (Figure 6) experimental measurement as well as numerical prediction shows that there is more uniform heating of the sample with even the bottom slices being heated by the penetrating microwaves and the temperatures at the corresponding slices compared to convection and radiant heating (Figures 4b–e) are higher as expected. The cycling of the microwaves can also be observed from the wavy nature of the computed temperature history plots. Moisture histories (Figures 7b–e) are similar for different slices, like for convection + radiant heating (Figures 5b–e). However, the amount of moisture loss is more compared to convection + radiant heating due to greater heating. The temperature maps showing spatial variations are now presented for a more detailed validation. Moisture maps are not shown as there is insignificant variation in the spatial distribution at any particular time, as discussed for Figures 5 and 7.

*Spatial Variation of Temperatures.* For a visualization of spatial variation of temperature in the samples, temperature maps at different slices obtained from computations and MRI after 10 min of heating are plotted in Figure 8. The computational model predicts the spatial temperature

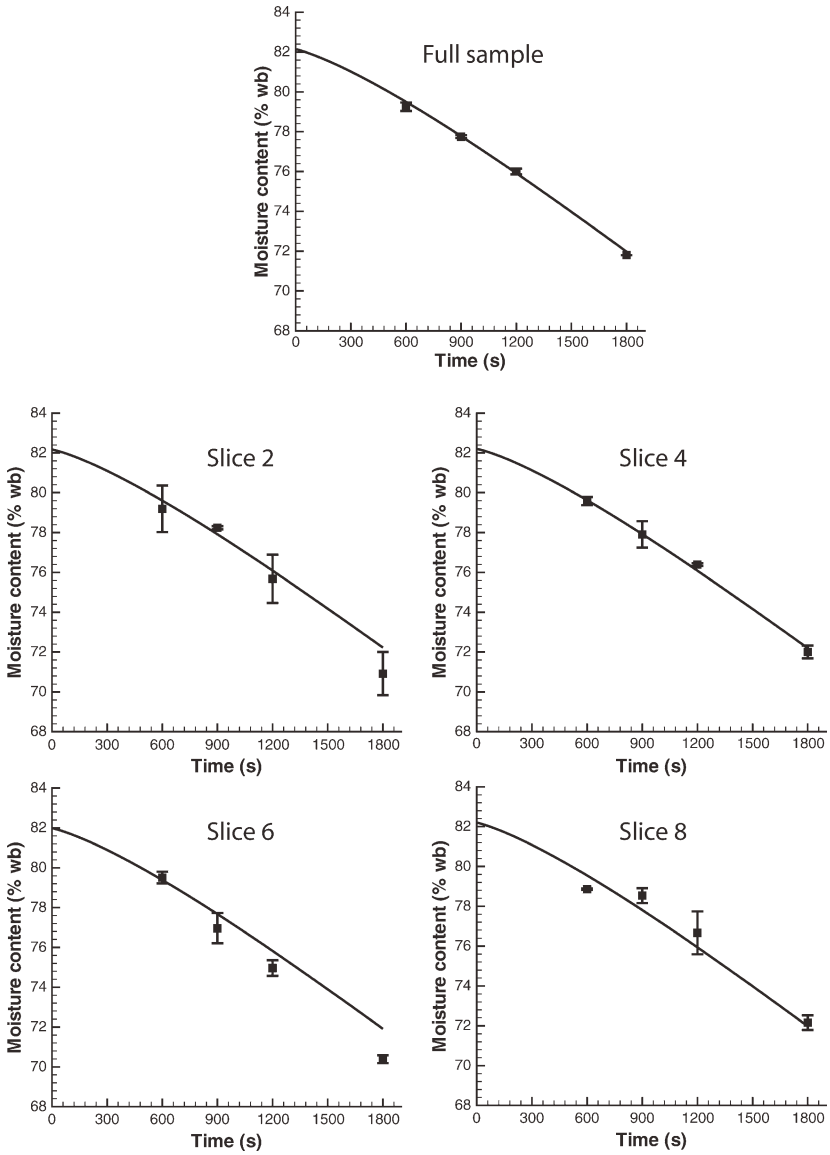


**Figure 7. Comparison of average moisture contents at different times obtained from computations and MRI experiments for the heating combination that involved convection, radiant heating and microwaves.**

The topmost plot shows the average moisture content comparison for the full sample and the other plots show the comparison for four different slices. MRI slice orientation is shown in Figure 3.

variations for the two different combinations as obtained experimentally from MRI accurately. The computed and MRI temperature maps for the two heating combinations both demonstrate two distinct features of heating: surface heating is seen in Figure 8 (top) for convection + radiant heating; and heating at the interior locations due to volumetric heating and focusing effect of the microwaves in addition to surface heating is observed in Figure 8 (bottom) for cycled microwave + convection + radiant heating. In the past, several researchers using simplified 1-D models (for waveguide studies) have demonstrated marked differences that exist between convection and microwave assisted heating, especially in relation to the volumetric or bulk heating phenomena.[37–39] Similar to rehydrated mashed potato samples used in the present work, brick, light concrete and wood considered in these past studies also had high moisture content. The interaction of electromagnetic fields with water, which has a high dielectric loss factor and is distributed throughout the wet material, leads to bulk heating of the samples. The focusing effect of the microwave was predominantly due to the cylindrical shape of the sample. Similar focusing effects have been observed for cylindrical food materials under microwave only heating in past MRI studies.[26,40]

### *Temperature distributions for different heating combinations*

Average temperature history for high vs. low initial moisture contents for different combination heating scenarios are shown in Figure 9. As expected, for a particular moisture content, heating rate increases as amount of microwave heating is increased. The temperatures are generally higher in

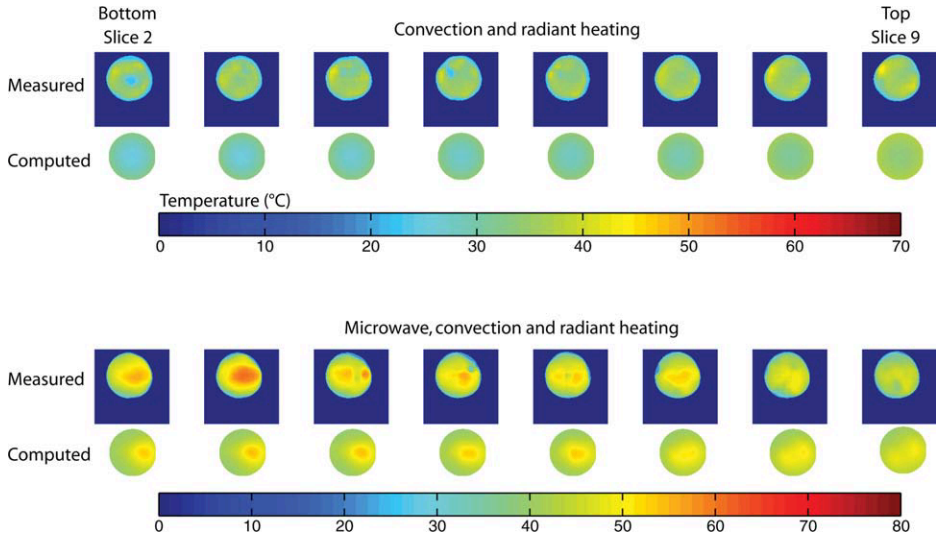


**Figure 8. Temperature maps comparing the measured (using MRI) and computed values at different slices in the samples after 10 min of heating.**

Details of the heating combinations are listed in Table 2. MRI slice orientation is shown in Figure 3. [Color figure can be viewed in the online issue, which is available at wileyonlinelibrary.com.]

the low initial moisture material for all heating combinations. Since the temperatures are higher for even the heating combination that does not include microwaves, higher temperature values observed in the initially drier product can be attributed to its lower specific heat capacity, 3410 J/kg K compared to 3726 J/kg K initially. The microwave deposition is comparable in magnitude, 4.21 W compared to 4.68 W at $t = 20$ min, since the electric field patterns do not change significantly as the dielectric properties change.

*High Initial Moisture Content.* The comparison between the spatial temperature values obtained in the material heated using different combinations for a high initial moisture material is shown in Figure 10. For convection and radiant heating, temperatures are high at the top surface since it is open. The sample also heats up from the sides but at a much lower rate (thermal resistance due to the mesh cylinder walls). When the microwaves are on for the full time, there is considerable rise in temperatures in the interior locations due to the focusing effect of the microwaves and the heating due to convection and radiation on the surface cannot catch up. It has been reported in past studies that internal temperatures during microwave heating may exceed the boiling point of water;[39] however, in this study such extreme values of temperatures were not observed due to the use of low power microwave heating. On the other hand, when cycled microwaves are added, although heating also takes place at the interior locations, the time available for conduction of heat when the microwaves are off leads to more uniform distribution of temperatures. As a result, there is no uncontrollable rise in temperatures in the interior and the sample is more uniformly heated. Thus cycling of microwaves can be used very effectively to complement convection and radiant heating to provide uniform heating to products during combination heating and, at the same time, for speeding up the heating process. The ratio of convection and radiant heating power to the microwave power absorbed by the sample is 5.8:1 for cycled and 1.2:1 for full microwaves. The convection and radiant heating power is calculated by integrating the surface heat flux over the sample surface. The microwave power absorbed is calculated using Eq. 9.

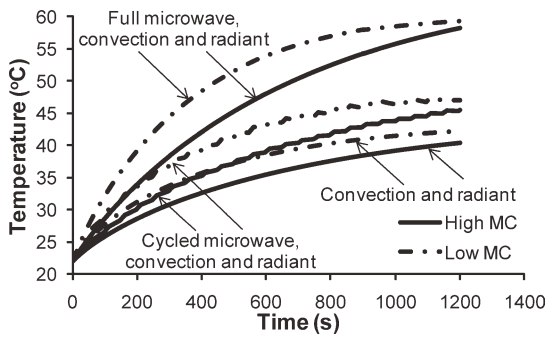


**Figure 9. Computed average temperature history for different initial moisture contents of the material, heated using three different combinations (listed in Table 2).**

Temperatures are generally higher in the low initial moisture samples for all heating combinations.

*Low Initial Moisture Content.* Figure 11 shows temperature distributions for the low initial moisture sample. Again in this case, microwaves become the dominant mode of heating when on for the full time and the surface does not get heated up as much. Cycled microwaves complement convection and radiant heating well for more uniform heating. The ratio of convection and radiant heating power to the microwave power absorbed by the sample is 4.6:1 for cycled and 0.7:1 for full microwaves.

### *Moisture distributions for different heating combinations*

Many safety (microbiological/chemical) and quality attributes of the final food product are related to the total

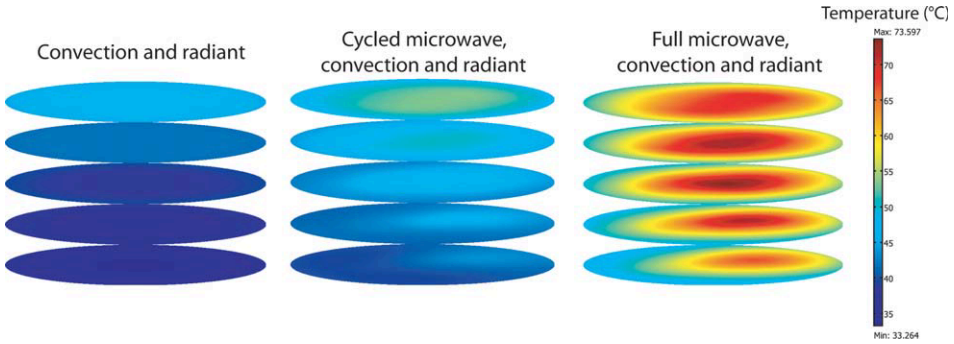


**Figure 10. Computed spatial temperature maps for material with high initial moisture content heated using different combinations (listed in Table 2) after 20 min of heating.**

For convection and radiant heating, temperatures are high at the top surface since it is open (as opposed to the sides that have lower convective heating due to presence of the mesh cylinder). Interior locations are heated by focusing effect for the two combinations that use microwaves. [Color figure can be viewed in the online issue, which is available at wileyonlinelibrary.com.]

moisture and moisture distribution after the heating/cooking process, making them critical information. The overall moisture losses from the samples heated by different combinations are shown in Figure 12. More moisture is lost from samples that are heated to higher temperatures since heating leads to increased evaporation and transport of water as water vapor in the porous medium. The moisture loss in 20 min from the high initial moisture samples are 7, 7.6, and 9.4% for convection and radiant, cycled microwave, convection and radiant, and full microwave, convection and radiant heating, respectively. For the low initial moisture samples, these are 15.4, 17.5, and 22.1%, respectively, showing a marked increase (more than two-fold) in the loss of moisture from the corresponding low initial moisture samples.

To determine the reason for the difference in moisture loss above, the total amount of water lost as liquid water and water vapor from the surface were calculated for the high and low moisture samples. For the high moisture sample heated using microwaves for the full time, the rate of loss of water as liquid and vapor was $3.02 \times 10^{-6}$ and $1.84 \times 10^{-7}$ kg/s, respectively, at $t = 20$ min. For the low moisture material, they were $1.36 \times 10^{-6}$ and $1.28 \times 10^{-6}$ kg/s, respectively. It can be observed that although the rate of water lost as liquid water reduces by half at low moisture content as the capillary diffusivity decreases (see Table 1), there is a 10-fold increase in moisture loss as vapor. This is attributed to the increase in temperatures as discussed for Figure 9 which leads to increased evaporation in the overall domain and the binary diffusion and pressure driven flow of vapor from the interior to surface.

*High Initial Moisture Content.* Figure 13 presents the moisture distribution in the high initial moisture samples after 20 min of heating. For convection and radiant heating, the moisture loss is mostly from the top surface with interior locations remaining at high moisture content even after 20 min of heating. The dominant mode of transport is capillarity which moves the liquid water to the surface and there is practically no pressure driven flow or binary diffusion of the vapor since the interior locations are not heated. The interior remains wet and the complete drying of the sample using only convective and radiant heating is therefore expected to take a very long time. In case of cycled microwave heating, there is additional mass transfer due to formation of vapor in the interior locations by evaporation and movement to the

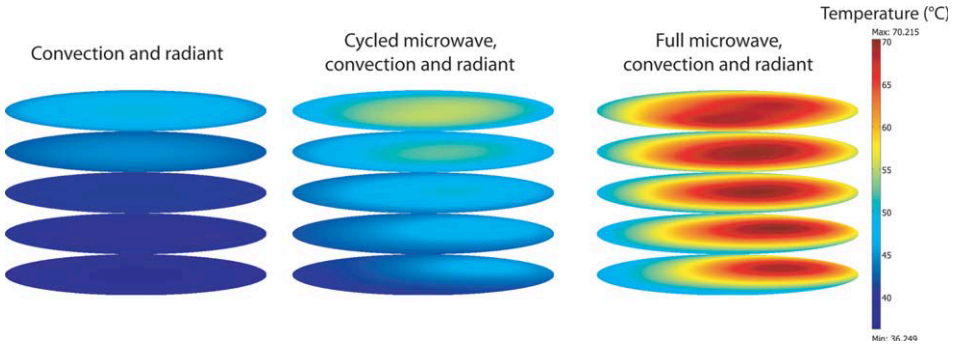


**Figure 11. Computed spatial temperature maps for material with low initial moisture content heated using different combinations (listed in Table 2) after 20 min of heating.**

Temperature distributions are qualitatively similar as for the high initial moisture case shown in Figure 10. [Color figure can be viewed in the online issue, which is available at wileyonlinelibrary.com.]

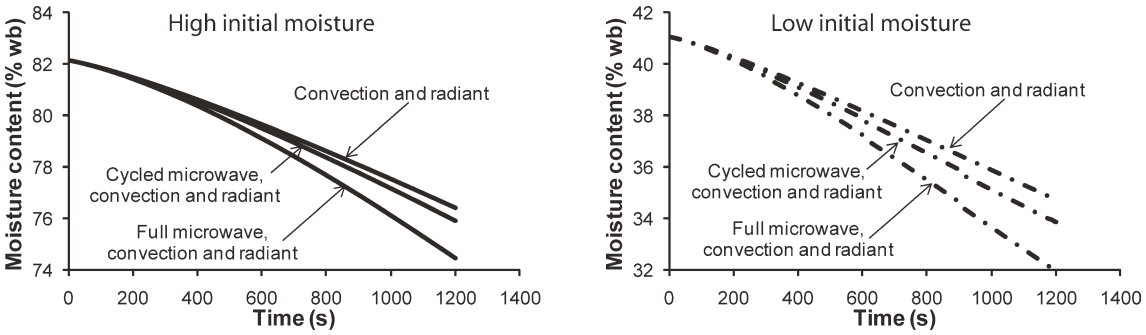


**Figure 12. Computed average moisture content history for material with different initial moisture contents heated using three different combinations (listed in Table 2).**

There is a marked increase (more than two-fold) in the loss of moisture from the low initial moisture samples compared to those starting at high moisture content due to increased evaporation.

surface by binary diffusion and pressure driven flow. Significant overpressures at the core of the material due to evaporation have similarly been attributed to volume heating nature of microwaves in past studies.[20,39] Using an empirical Lambert-Beer law for microwave absorption in a 1-D approximation, it was shown that these overpressures boost transfer of water from the core of the porous material to the surface,[20] similar to water transport observed during cycled microwave heating in this study.

When the microwaves are on for the full time, very high heating rates are involved and there is increased evaporation leading to comparable moisture loss in the interior locations as well. In certain locations though, the moisture loss from the surface is not able to keep up with additional moisture coming from interior and therefore the locations close to the surface have higher moisture content. This is generally not desired during food preparation since it leads to soggy surface and is one of the known drawbacks of microwave-only heating. This accumulation of vapor at the edges has also been reported in wood drying studies.[12] Interestingly, this is not observed when cycled microwaves are added and hence, careful addition of heating modes by matching the relative rates of heating may help in development of custom products by keeping the surface moisture low (crisp).

*Low Initial Moisture Content.* For the low initial moisture material, there is more variation in the moisture distribution even for convection and radiant heating (Figure 14). This is attributed to higher evaporation in the low moisture material discussed earlier. An interesting result observed here is that even when the microwaves are on for the full time, there is no accumulation of moisture in the surface unlike the high moisture material. In this case, the rate of evaporation of moisture due to convection and radiant heating near the surface becomes higher than that due to microwave heating which in turn facilitates moisture removal from the surface. This phenomena is also discussed in the next section.

### *Pressure distributions for different heating combinations*

*High Initial Moisture Content.* Pressure distributions (Figure 15) show that in convection and radiant heating negative pressures (minimum value of −57 Pa) are developed in the interior locations due to condensation of vapor (the reported pressures are relative to atmosphere). Similar underpressures (−8 to −100 Pa) have been reported in the early stages of convective drying of wood due to condensation.[20,39] Very small positive pressures (maximum value of

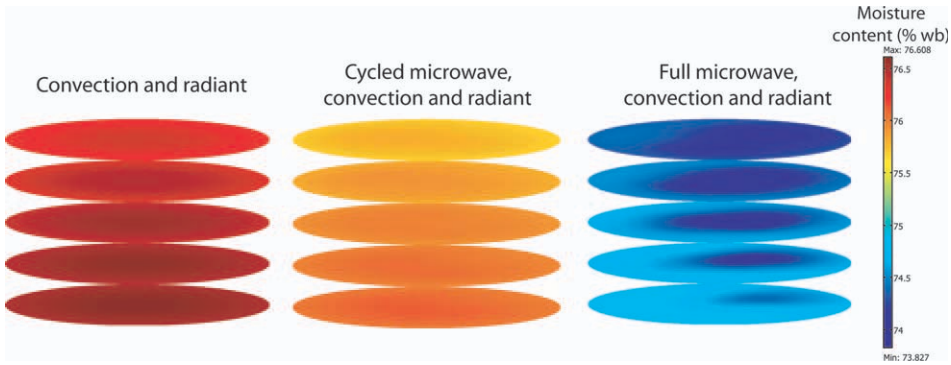


**Figure 13. Computed moisture content maps for material with high initial moisture content heated using different combinations (listed in Table 2) after 20 min of heating.**

In case of convection and radiant heating, moisture is lost mostly from the surface (shown by lighter shades of red), whereas in case of full microwaves, there is accumulation of moisture at the surface (as represented by lighter shades of blue). For cycled microwaves, a more uniform moisture loss is seen. [Color figure can be viewed in the online issue, which is available at wileyonlinelibrary.com.]

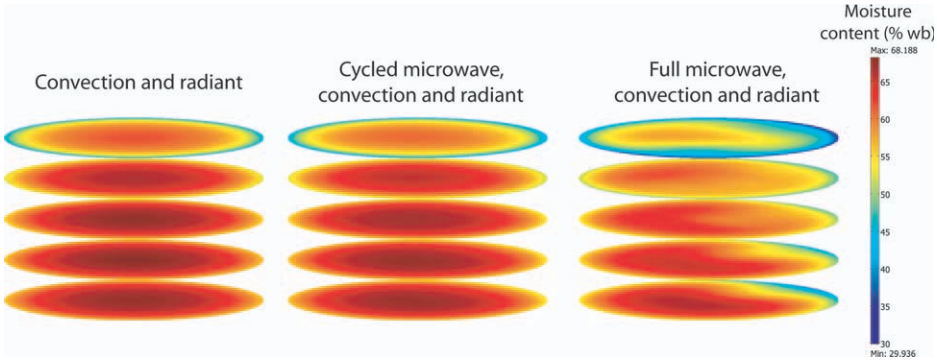


**Figure 14. Computed moisture content maps for material with low initial moisture content heated using different combinations (listed in Table 2) after 20 min of heating.**

No accumulation of surface moisture, as opposed to the high moisture case (Figure 13), is seen even when microwaves are on for the full time. [Color figure can be viewed in the online issue, which is available at wileyonlinelibrary.com.]

0.375 Pa) are observed close to the surface due to evaporation. In case of cycled microwaves, pressures are mostly positive in the domain (maximum value of 50.8 Pa); however, there are a few spots which have negative pressure (minimum value of −6.51 Pa) indicating condensation. Very high pressures are observed in the interior locations (maximum value of 845.7 Pa) and the pressures are positive throughout the domain when the microwaves are on for the full time as a result of the high microwave heating rate. These overpressures due to evaporation as a result of volumetric microwave heating are also consistent with previously reported values (200–1000 Pa).[20] A general trend is therefore seen here that convection and radiant heating leads to negative pressure development in the core of the domain due to condensation whereas during microwave heating, the pressures are generally positive due to evaporation.

*Low Initial Moisture Content.* In case of low moisture material (Figure 16), although there is negative pressure development in the core region (minimum value of −29.9 Pa), the positive pressures near the surface (maximum value of 4 Pa) are higher which supports the fact that there is greater evaporation near the surface in low moisture material as discussed earlier for moisture profiles. For cycled microwave heating and with microwaves on for the full time, pressures are positive throughout the domain with maximum values of 72.3 Pa and 615.5 Pa, respectively. As in the high moisture case, evaporation (due to bulk microwave heating) leads to overpressures whereas condensation in the core (in absence of volumetric heating) leads to underpressures in the low moisture material. The pressure magnitudes are also consistent with past studies.[20,39]

## Summary and Conclusions

In this work, combination heating was studied the most comprehensive way, using a novel synergy of physics-based computation and MRI experimentation. This is also the first study that uses complex coupling of Maxwell's equations of electromagnetics in 3-D with a multiphase porous media model to study combination heating. The coupling of different physics and MRI measurements both present unmatched computational and experimental challenges. The use of such a technique is, however, required in the study of combination heating processes, otherwise predictions of critical parameters such as microwave energy deposition, temperature, moisture content and pressure in space and time are not possible. Knowledge of these factors can, in turn, lead to a quantum improvement in speed, quality and safety of food preparation, increased ability of automation and customization, retention of food nutrition and organoleptic qualities,

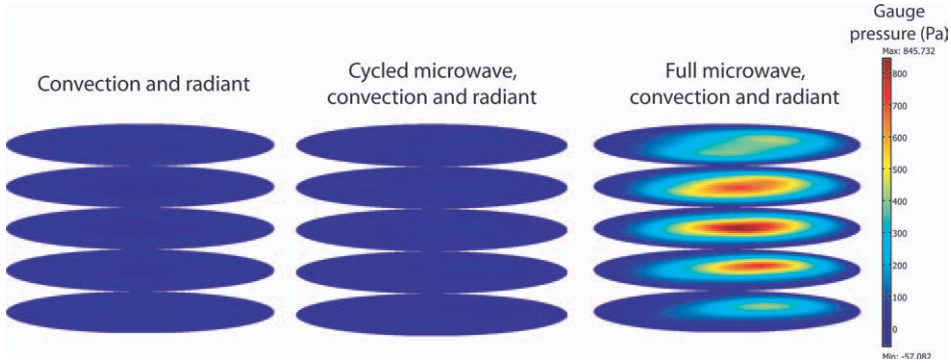


**Figure 15. Computed pressure distributions for material with high initial moisture content heated using different combinations (listed in Table 2) after 20 min of heating.**

Convection and radiant heating leads to negative pressure development in the core of the domain whereas during microwave heating, the pressures are generally positive. [Color figure can be viewed in the online issue, which is available at wileyonlinelibrary.com.]

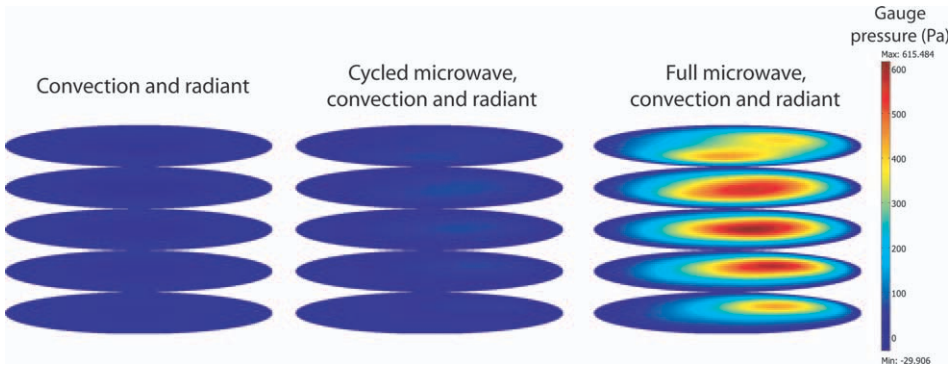


**Figure 16. Computed pressure distributions for material with low initial moisture content heated using different combinations (listed in Table 2) after 20 min of heating.**

Pressure distributions are similar to the high moisture case shown in Figure 15. [Color figure can be viewed in the online issue, which is available at wileyonlinelibrary.com.]

reduction of food wastage, and increase of energy efficiency. It may be pointed out that due to the large number of parameters needed in the complex model, quantification of model sensitivity to different parameters may be important. An uncertainty analysis, following the work of Rabin (2003),[41] may be performed for estimating the uncertainty in model variables due to changes in the input parameters and will be considered as a future work.

The key conclusions from the work are summarized as follows. (1) For a combination heating process that includes microwaves, distribution of parameters such as temperature and moisture content in 3-D were obtained that are critical to comprehensively understand and optimize the process. (2) More specifically, microwaves complement the convection and radiant heating regimes well. Also different mass transfer mechanisms were found to be dominant for different heating combinations, i.e., capillary flow for convective and radiant heating and pressure driven and binary diffusion for microwave heating. However, matching of relative power from convection and radiant heating and microwaves is extremely critical to obtain a balanced heating rate in the material and to avoid formation of extreme regions of high-temperature or excessive moisture. Generally the combination heating process provides uniform heating when the relative microwave power is substantially lower than the power due to convective and radiant heating. (3) High and low moisture materials behave differently under microwave combination heating. Higher temperatures and moisture loss were observed for low moisture material. It was found that low moisture materials can be heated uniformly using higher microwave power which is not possible in high moisture material. Therefore, these factors must be taken into consideration before designing a combination heating process. (4) Cycling of microwave is useful in distribution of excessive volumetric heat by microwaves and can increase the effectiveness of the combination heating process.

## Acknowledgments

This project was supported by National Research Initiative Grant no. 2003-35503-13737 from the USDA Cooperative State Research, Education, and Extension Service Competitive Grants program. The authors also acknowledge Amit Halder (Dept. of Biological and Environmental Engineering, Cornell University, Ithaca, NY) for providing the initial simulation files and Youngseob Seo (Dept. of Biomedical Engineering, University of California, Davis, CA) for work in the initial part of the MRI measurement.

## Notation

$B_o$ = magnetic field strength, T
$c$ = concentration, kg m$^{-3}$
$c_p$ = specific heat capacity, J kg$^{-1}K^{-1}$
$C$ = molar density, kmol m$^{-3}$
$D_{\text{eff},\,g}$ = effective gas diffusivity, m$^2s^{-1}$
$D$ = capillary diffusivity, m$^2s^{-1}$
$\mathbf{E}$ = electric field intensity, V m$^{-1}$
$h$ = heat transfer coefficient, W m$^{-2}K^{-1}$
$h_m$ = mass transfer coefficient of vapor, ms$^{-1}$
$\mathbf{H}$ = magnetic field intensity, A m$^{-1}$
$i$ = imaginary unit, $\sqrt{-1}$
$\dot{I}$ = volumetric evaporation rate, kgm$^{-3}s^{-1}$
$j$ = total mass flux, kg m$^{-2}s^{-1}$
$k^{\text{th}}$ = thermal conductivity, Wm$^{-2}K^{-1}$
$k$ = intrinsic permeability, m$^2$
$k_r$ = relative permeability
$K$ = non-equilibrium evaporation constant
$m$ = overall mass fraction
$M$ = moisture content, db
$M_a$, $M_v$ = molecular weight of air and vapor
$n$ = normal direction
$P$, $p$ = total pressure and partial pressure, respectively, Pa
$q$ = heat flux, W m$^{-2}$
$Q$ = microwave source term, Jm$^{-3}s^{-1}$
$R$ = universal gas constant, J kmol$^{-1}$ K$^{-1}$
$S$ = saturation
$t$ = time, s
$T$ = Temperature, °C
$TE$ = echo time, s
$\mathbf{v}$ = velocity, m s$^{-1}$
$V$ = volume, m$^3$
$x$,$y$,$z$ = directions, m

### *Greek letters*

$\alpha$ = proportionality constant, ppm/°C
$\gamma$ = magnetogyric ratio of hydrogen nucleus, rad/s T
$\rho$ = density, kg m$^{-3}$
$\lambda$ = latent heat of vaporization, J kg$^{-1}$
$\omega_a$, $\omega_v$ = mass fraction of vapor and air with respect to total gas
$\phi$ = porosity
$\mu$ = dynamic viscosity, Pa s
$\epsilon_0$ = permittivity of free space, $8.854 \times 10^{-12}$ Fm$^{-1}$
$\mu_0$ = permeability of free space, $4\pi \times 10^{-7}$ Hm$^{-1}$
$\epsilon$ = complex relative permittivity

$\epsilon'$ = dielectric constant
$\epsilon''$ = dielectric loss
$\omega$ = angular frequency, rad $s^{-1}$
$\varphi$ = phase shift, rad

## Literature Cited


1. Datta AK, Geedipalli SSR, Almeida MF. Microwave combination heating. *Food Technol*. 2005;59:36–40.
2. Makoviny I, Zemiar J. Heating of wood surface layers by infrared and microwave radiation. *Wood Res*. 2004;49:33–40.
3. Huang ZJ, Gotoh M, Hirose Y. Improving sinterability of ceramics using hybrid microwave heating. *J Mater Process Technol*. 2009;209:2446–2452.
4. McMinn WAM, McLoughlin CM, Magee TRA. Thin-layer modeling of microwave, microwave-convective, and microwave-vacuum drying of pharmaceutical powders. *Drying Technol*. 2005;23:513–532.
5. Vongpradubchai S, Rattanadecho P. The microwave processing of wood using a continuous microwave belt drier. *Chem Eng Process*. 2009;48:997–1003.
6. Rakesh V, Datta AK, Amin MHG, Hall LD. Heating uniformity and rates in a domestic microwave combination oven. *J Food Process Eng*. 2009;32:398–424.
7. Wappling-Raaholt B, Scheerlinck N, Galt S, Banga JR, Alonso A, Balsa-Canto E, Van Impe J, Ohlsson T, Nicolai BM. A combined electromagnetic and heat transfer model for heating of foods in microwave combination ovens. *J Microwave Power Electromagn Energy*. 2002;37:97–111.
8. Durairaj S, Basak T. Analysis of pulsed microwave processing of polymer slabs supported with ceramic plates. *Chem Eng Sci*. 2009;64:1488–1502.
9. Rakesh V, Seo Y, Datta AK, McCarthy KL, McCarthy MJ. Heat transfer during microwave combination heating: computational modeling and MRI experiments. *AIChE J*. 2010;56:2468–2478.
10. Basak T. Role of various elliptical shapes for efficient microwave processing of materials. *AIChE J*. 2007;53:1399–1412.
11. Curet S, Rouaud O, Boillereaux L. Effect of sample size on microwave power absorption within dielectric materials: 2D numerical results vs. closed-form expressions. *AIChE J*. 2009;55:1569–1583.
12. Hansson L, Antti L. Modeling microwave heating and moisture redistribution in wood. *Drying Technol*. 2008;26:552–559.
13. Brodie G. Simultaneous heat and moisture diffusion during microwave heating of moist wood. *Appl Eng Agric*. 2007;23:179–187.
14. Sharma GP, Prasad S, Chahar VK. Moisture transport in garlic cloves undergoing microwave-convective drying. *Food Bioproducts Process*. 2009;87:11–16.
15. Halder A, Dhall A, Datta AK. An improved, easily implementable, porous media based model for deep-fat frying — Part I: model development and input parameters. *Food Bioproducts Process*. 2007;85:209–219.
16. Ni H, Datta AK. Moisture, oil and energy transport during deep-fat frying of food materials. *Food Bioproducts Process*. 1999;77:194–204.
17. Yamsaengsung R, Moreira RG. Modeling the transport phenomena and structural changes during deep fat frying — part 1: model development. *J Food Eng*. 2002;53:1–10.
18. Turner IW, Perre P. Vacuum drying of wood with radiative heating: II. Comparison between theory and experiment. *AIChE J*. 2004;50:108–118.
19. Ni H, Datta AK, Torrance KE. Moisture transport in intensive microwave heating of biomaterials: a multiphase porous media model. *Int J Heat Mass Transfer*. 1999;42:1501–1512.
20. Salagnac P, Glouannec P, Lecharpentier D. Numerical modeling of heat and mass transfer in porous medium during combined hot air, infrared and microwaves drying. *Int J Heat Mass Transfer*. 2004;47:4479–4489.
21. Groombridge P, Oloyede A, Siores E. A control system for microwave processing of materials. *J Manuf Sci Eng Trans ASME*. 2000;122:253–261.
22. Roussy G, Bennani A, Thiebaut JM. Temperature runaway of microwave irradiated materials. *J Appl Phys*. 1987;62:1167–1170.
23. Liu CM, Wang QZ, Sakai N. Power and temperature distribution during microwave thawing, simulated by using Maxwell's equations and Lambert's law. *Int J Food Sci Technol*. 2005;40:9–21.
24. Akkari E, Chevallier S, Boillereaux L. Observer-based monitoring of thermal runaway in microwaves food defrosting. *J Process Control*. 2006;16:993–1001.
25. McCarthy MJ. *Magnetic Resonance Imaging in Foods*. New York, NY: Chapman and Hall, Inc. 1994.
26. Nott KP, Hall LD. Validation and cross-comparison of MRI temperature mapping against fibre optic thermometry for microwave heating of foods. *Int J Food Sci Technol*. 2005;40:723–730.
27. Haala J, Wiesbeck W. Modeling microwave and hybrid heating processes including heat radiation effects. *IEEE Trans Microwave Theory Tech*. 2002;50:1346–1354.
28. Geedipalli SSR, Rakesh V, Datta AK. Modeling the heating uniformity contributed by a rotating turntable in microwave ovens. *J Food Eng*. 2007;82:359–368.
29. Ghosh PK, Jayas DS, Smith EA, Gruwel MLH, White NDG, Zhilkin PA. Mathematical modelling of wheat kernel drying with input from moisture movement studies using magnetic resonance imaging (MRI), Part I: model development and comparison with MRI observations. *Biosyst Eng*. 2008;100:389–400.
30. Hwang SS, Cheng YC, Chang C, Lur HS, Lin TT. Magnetic resonance imaging and analyses of tempering processes in rice kernels. *J Cereal Sci*. 2009;50:36–42.
31. MacMillan B, Hickey H, Newling B, Ramesh M, Balcom B. Magnetic resonance measurements of French fries to determine spatially resolved oil and water content. *Food Res Int*. 2008;41:676–681.
32. Bear J. *Dynamics of Fluids in Porous Media*. New York, NY: Dover Publications 1972.
33. Datta AK. Porous media approaches to studying simultaneous heat and mass transfer in food processes. I: problem formulations. *J Food Eng*. 2007;80:80–95.
34. Choi Y, Okos MR. *Thermal properties of liquid foods review*. In: Okos MR editor. *Physical and Chemical Properties of Food* St Joseph, MI: American Society of Agricultural Engineers. 1986:35–77.
35. Ratti C, Crapiste GH, Rotstein E. A new water sorption equilibrium expression for solid foods based on thermodynamic considerations. *J Food Sci*. 1989;54:738–747.
36. Callaghan PT. *Principles of Nuclear Magnetic Resonance Microscopy*. Oxford: Clarendon Press. 1991:492.
37. Constant T, Perre P, Moyne C. Drying with internal heat generation: theoretical aspects and application to microwave heating. *AIChE J*. 1996;42:359–368
38. Turner IW, Jolly PG. Combined microwave and convective drying of a porous material. *J Drying Technol*. 1991;9:1209–1270.
39. Perre P, Turner IW. Microwave drying of softwood in an oversized waveguide: theory and experiment. *AIChE J*. 1997;43:2579–2595.
40. Bows JR, Patrick ML, Nott KP, Hall LD. Three-dimensional MRI mapping of minimum temperatures achieved in microwave and conventional food processing. *Int J Food Sci Technol*. 2001;36:243–252.
41. Rabin Y. A general model for the propagation of uncertainty in measurements into heat transfer simulations and its application to cryosurgery. *Cryobiology*. 2003;46:109–120.


*Manuscript received Aug. 25, 2010, revision received Feb. 2, 2011, and final revision received Apr. 12, 2011.*